The effects of drag on turbulent gravity currents

By L Y N N E   H A T C H E R[1], A N D R E W   J.   H O G G[1]
AND A N D R E W   W.   W O O D S[2]

[1]Centre for Environmental and Geophysical Flows, School of Mathematics,
University of Bristol, Bristol, BS8 1TW UK

[2]BP Institute, University of Cambridge, Madingley Road, Cambridge CB3 0EZ, UK

We model the propagation of turbulent gravity currents through an array of obstacles which exert a drag force on the flow proportional to the square of the flow speed. A new class of similarity solutions is constructed to describe the flows that develop from a source of strength $q_0 t^\gamma$. An analytical solution exists for a finite release, $\gamma = 0$, while power series solutions are developed for sources with $\gamma > 0$. These are shown to provide an accurate approximation to the numerically calculated similarity solutions. The model is successfully tested against a series of new laboratory experiments which investigate the motion of a turbulent gravity current through a large flume containing an array of obstacles. The model is extended to account for the effects of a sloping boundary. Finally, a series of geophysical and environmental applications of the model are discussed.

1. Introduction

There are several situations in which gravity-driven flows at high Reynolds number encounter obstacles or roughness elements which impede the progress of the current. Important examples include high-Reynolds-number flows in rough-walled fractures, dilute powder snow avalanches propagating through arrays of retarding mounds (Jóhannesson *et al.* 1996), large-scale dense gas flows through wooded or built-up areas and density currents flowing down continental shelves (Lane-Serff 1993). In permeable fractured rock, the near-surface transport of water is often controlled by large fractures. If the aperture is sufficiently wide, then the Reynolds number of this flow based on aperture width may exceed 100. In this case, the roughness of the walls leads to a net drag force proportional to the square of the velocity, and this force dominates the viscous drag (Dullien 1991; Bear 1988). Dilute powder snow avalanches have been responsible for serious damage to a number of towns in Iceland and in Switzerland located at the foot of steep slopes (Jóhannesson *et al.* 1996). In order to mitigate such disasters, a variety of defence structures have been built. One system involves an array of retarding mounds designed to arrest the flow by reducing its speed and thereby facilitating the deposition of snow upstream of a settlement. For high-Reynolds-number powder snow avalanches (Hopfinger 1983), such mounds can exert a drag force proportional to the square of the flow speed. Finally, we note that large dense gas releases produced from industrial accidents may encounter natural or man-made obstacles which again impart a turbulent drag on the current proportional to the square of the flow speed.

In order to develop some insight into the physical controls on the propagation

of turbulent gravity-driven flows through such arrays of obstacles, we explore an idealized model in which the presence of the obstacles is modelled by a uniform drag force proportional to the square of the velocity and inversely proportional to the mean length scale of the obstacles. We find that the frictional force causes the flow to evolve away from the classical buoyancy–inertia balance which applies at early times and which has been described in detail by numerous workers (Rottman & Simpson 1983; Gratton & Vigo 1994). Instead, a new long-time asymptotic balance is established between the buoyancy force and the turbulent drag. We develop a new class of similarity solutions to describe the motion of such currents following instantaneous and continuous releases of fluid. We then present the results of a new series of experiments to test this model. In the experiments, we examined the motion of a saline gravity current propagating through a 3 m long flume in which a regular array of vertical obstacles produced a turbulent drag throughout the current. We extend the model to include the effects of a sloping boundary and conclude with a discussion of several applications of the model.

It is worth noting that Rottman *et al.* (1985) examined the impact of a localized porous barrier on the propagation of a gravity current. In that case the porous barrier partially arrests the flow: a fraction seeps through the obstacle and continues downstream as an inertial current while a part is blocked by the obstacle leading to the upstream propagation of a weak hydraulic jump (cf. Lane-Serff, Beal & Hadfield 1995). In contrast to that work this present study is concerned with the propagation of a gravity current through a spatially extensive (rather than localized) porous layer so that the turbulent drag associated with the porous layer can dominate the dynamics. In a theoretical contribution Lane-Serff (1993) examined the steady-state dynamics of a current propagating down a slope. The current was subject to turbulent entrainment of the ambient fluid on its upper surface, turbulent drag and deceleration due to the structure of the ambient fluid. This earlier study is complementary to the present paper, in which we consider the transient motion of a gravity current produced from a finite release and examine motion on both horizontal and inclined surfaces. In both studies the motion is governed by a balance between the buoyancy force and turbulent drag.

2. Turbulent drag acting on a unidirectional gravity current

When a high-Reynolds-number flow of speed u passes an obstacle of width d a drag force is exerted on the flow of the form $c_D \rho u^2 A$, where $A = hd$ is the cross-sectional area of the obstacle in the flow and the drag coefficient c_D depends on the detailed shape of the obstacle, Rouse (1961). For a flow of depth $h(\gg d)$, propagating through an array of such obstacles, with volume fraction $\phi(\ll 1)$, we expect the drag force on the current, per unit area in the direction of the flow, to scale as $c_D \rho u^2 A \phi/a$ where a is the area of each obstacle in plan. For the two-dimensional propagation of a long thin Boussinesq current along a horizontal boundary through a deep layer of water we may adopt the depth-averaged single-layer shallow-water model (e.g. Gill 1982). If we include the turbulent drag force then the momentum equation in the flow direction, x, has the form

$$\frac{\partial u}{\partial t} + u \frac{\partial u}{\partial x} = -\lambda u|u| - g' \frac{\partial h}{\partial x}, \qquad (2.1)$$

where $\lambda = c_D \phi/d$ and the reduced gravity $g' = (\rho_c - \rho_a)g/\rho_a$ is defined in terms of the densities ρ_c and ρ_a of the current and ambient fluid respectively and the

gravitational acceleration g. As the current advances, we anticipate that, as with inertially dominated gravity currents flowing over horizontal boundaries, the mass of fluid entrained into the flow will be small (Simpson 1997), and later in the paper we show that this is approximately the case in our experiments. In the absence of entrainment, the depth-integrated mass-continuity equation has the form

$$\frac{\partial h}{\partial t} + \frac{\partial}{\partial x}(uh) = 0. \tag{2.2}$$

This expression for mass conservation in the absence of entrainment follows the approach of a number of investigations of gravity current flow over horizontal boundaries (Rottman & Simpson 1983; Gratton & Vigo 1994). When there is a significant slope, however, the entrained flux of fluid may be parameterized as a function of the Richardson number of the flow, $Ri = g'h/u^2$. For example, Ellison & Turner (1959) found the entrainment to be a decreasing function of the Richardson number. Thus flows with large Richardson number exhibit relatively little mixing with the overlying ambient fluid. In this study we predominately examine the motion of shallow and laterally extensive currents over horizontal boundaries for which entrainment has been found to be of little significance and we find that the effects of drag are to slow and deepen the flow, thus increasing the Richardson number and further suppressing entrainment.

In the remainder of the paper, we consider gravity currents with total volume

$$q(t) = q_0 t^\gamma \tag{2.3}$$

per unit distance cross-stream, where $\gamma > 0$. The currents are released from a line source, $x = 0$, for times $t > 0$, and propagate into the region $x > 0$, hence $u > 0$. In the Appendix, analogous results are presented for an axisymmetric current generated by a point source of dense fluid. Scaling analysis identifies that there is a critical time, t_c say, at which the turbulent drag and the flow inertia are of comparable magnitude given by the physical balances

$$\frac{u}{t_c} \sim \lambda u^2 \sim \frac{g'h}{ut_c}, \tag{2.4}$$

where

$$hut_c \sim q_0 t_c^\gamma. \tag{2.5}$$

This leads to the scaling

$$t_c \sim \left(\lambda^3 q_0 g'\right)^{-1/(\gamma+2)}. \tag{2.6}$$

As the flow evolves, two dynamical regimes emerge depending upon whether $t \ll t_c$ or $t \gg t_c$. At short times, $t \ll t_c$, there is a balance between the inertia and the buoyancy forces,

$$\frac{\partial u}{\partial t} + u\frac{\partial u}{\partial x} \sim -g'\frac{\partial h}{\partial x}, \tag{2.7}$$

leading to the classic solutions for an inertial gravity current (Hoult 1972; Rottman & Simpson 1983). At longer times, $t \gg t_c$, the flow evolves from this regime, and we will show in equation (3.10) that a new balance emerges in equation (2.1) between the turbulent drag and the buoyancy force driving the flow,

$$-\frac{c_D}{d}u^2\phi = g'\frac{\partial h}{\partial x}. \tag{2.8}$$

The purpose of this work is to examine the flows that develop in this long-time, $t \gg t_c$, turbulent drag dominated regime.

3. Similarity solutions: $t \gg t_c$

For a source flux of the form (2.3), we expect the flow to become self-similar, with the depth and speed taking the form

$$h(x,t) = aH[\omega t]^{\alpha} \mathscr{F}(\eta), \tag{3.1}$$

$$u(x,t) = bH\omega[\omega t]^{\mu} \mathscr{G}(\eta), \tag{3.2}$$

where the similarity variable η is defined as

$$\eta = \frac{x}{X_0 H[\omega t]^{\beta}}. \tag{3.3}$$

$\mathscr{F}(\eta)$ and $\mathscr{G}(\eta)$ are the shape factors which determine the depth and speed of the current as a function of position in the flow. Also, a, b and X_0 are dimensionless constants where X_0 is chosen so that the leading edge of the current, $h = 0$, is located at $\eta = 1$. H and $1/\omega$ are characteristic depths and time scales of the flow given by

$$H = q_0^{1/(2-\gamma)} \left(\frac{g'}{\lambda}\right)^{\gamma/[2(\gamma-2)]} \tag{3.4}$$

and

$$\omega = \left(\frac{\lambda q_0}{g'}\right)^{1/(\gamma-2)}. \tag{3.5}$$

Matching the exponents of time in the equations for local (2.2) and global (2.3) mass conservation, and in the dynamic equation (2.8), we deduce that

$$\alpha = \tfrac{3}{4}\gamma - \tfrac{1}{2}, \quad \beta = \tfrac{1}{2} + \tfrac{1}{4}\gamma \quad \text{and} \quad \mu = \tfrac{1}{4}\gamma - \tfrac{1}{2}. \tag{3.6}$$

For convenience we set

$$a = X_0^3 \quad \text{and} \quad b = X_0 \tag{3.7}$$

so that, in terms of the similarity variables, the shape factors $\mathscr{F}(\eta)$ and $\mathscr{G}(\eta)$ are governed by the dimensionless equations

$$\left(\tfrac{3}{4}\gamma - \tfrac{1}{2}\right)\mathscr{F} - \left(\tfrac{1}{2} + \tfrac{1}{4}\gamma\right)\eta \frac{d\mathscr{F}}{d\eta} + \frac{d}{d\eta}(\mathscr{F}\mathscr{G}) = 0 \tag{3.8}$$

from (2.2) and

$$\frac{d\mathscr{F}}{d\eta} = -\mathscr{G}^2 \tag{3.9}$$

from (2.8). As a check in the scalings which lead to (2.8) it may be seen that substitution of the similarity solutions into the full dynamic equation (2.1) leads to the balance

$$\frac{1}{X_0}\left(\frac{t_c}{t}\right)^{1/2+\gamma/4} \left(-\left(\tfrac{1}{2} + \tfrac{1}{4}\gamma\right)\frac{d\mathscr{G}}{d\eta}\eta + \left(\tfrac{1}{4}\gamma - \tfrac{1}{2}\right)\mathscr{G} + \mathscr{G}\frac{d\mathscr{G}}{d\eta}\right) + \frac{d\mathscr{F}}{d\eta} = -\mathscr{G}^2 \tag{3.10}$$

which reduces to (3.9) when $t \gg t_c$. The global conservation of mass (2.3) leads to the integral condition

$$X_0 = \left(\int_0^1 \mathscr{F}\,d\eta\right)^{-1/4}. \tag{3.11}$$

Finally, at the front of the current, $x = x_N(t)$, the kinematic boundary condition

$$\frac{\mathrm{d}x_N}{\mathrm{d}t} = u(x_N) \tag{3.12}$$

requires that

$$\mathcal{G}(1) = \tfrac{1}{2} + \tfrac{1}{4}\gamma. \tag{3.13}$$

By solving equations (3.8), (3.9) we then have the similarity solutions of the form

$$h(x,t) = X_0^3 q_0^{3/4} \left(\frac{\lambda}{g'}\right)^{1/4} t^{3\gamma/4 - 1/2} \mathcal{F}(\eta) \tag{3.14}$$

and

$$u(x,t) = X_0 \left(\frac{g' q_0}{\lambda}\right)^{1/4} t^{\gamma/4 - 1/2} \mathcal{G}(\eta), \tag{3.15}$$

where the similarity variable, η, is given by

$$x = \eta X_0 \left(\frac{q_0 g'}{\lambda}\right)^{1/4} t^{1/2 + \gamma/4}. \tag{3.16}$$

We now consider the solutions of $\mathcal{F}(\eta)$ and $\mathcal{G}(\eta)$ for the cases of (i) a finite release of fluid; and (ii) a maintained source of fluid.

3.1. *The finite release: $\gamma = 0$*

For a finite release, $\gamma = 0$, we can find explicit solutions for $\mathcal{F}$ and $\mathcal{G}$. Equation (3.8) may be rewritten as

$$\frac{\mathrm{d}}{\mathrm{d}\eta}(\mathcal{F}\eta) = 2\frac{\mathrm{d}}{\mathrm{d}\eta}(\mathcal{F}\mathcal{G}). \tag{3.17}$$

Integrating once and using $u(0) = 0$, and hence $\mathcal{G}(0) = 0$, we find that

$$\mathcal{G} = \tfrac{1}{2}\eta \tag{3.18}$$

so that the speed increases linearly with distance from the source. Now substituting (3.18) into (3.9) gives

$$\frac{\mathrm{d}\mathcal{F}}{\mathrm{d}\eta} = -\tfrac{1}{4}\eta^2 \Rightarrow \mathcal{F} = -\tfrac{1}{12}\eta^3 + A, \tag{3.19}$$

where A is a constant. The condition $\mathcal{F}(1) = 0$ implies that $A = 1/12$ and so

$$\mathcal{F} = \tfrac{1}{12}(1 - \eta^3). \tag{3.20}$$

Global conservation of mass (2.3) then indicates that $X_0 = 2$. In figure 1 we illustrate the form of $\mathcal{F}(\eta)$ and $\mathcal{G}(\eta)$.

3.2. *The maintained source: $\gamma > 0$*

In the case $\gamma > 0$, the shape of the current may be calculated exactly by solving the shape equations (3.8), (3.9) numerically subject to the boundary conditions given above. For example in figure 2(a), we illustrate the form of the solution for $\gamma = 1$. However, it is worth noting that since the current has depth $\mathcal{F} = 0$ at its nose, $\eta = 1$, we can develop accurate power series solutions for $\mathcal{F}$ and $\mathcal{G}$ of the form

$$\mathcal{F}(\eta) = c_0 + c_1(1 - \eta) + c_2(1 - \eta)^2 + \cdots, \tag{3.21}$$

$$\mathcal{G}(\eta) = d_0 + d_1(1 - \eta) + d_2(1 - \eta)^2 + \cdots \tag{3.22}$$
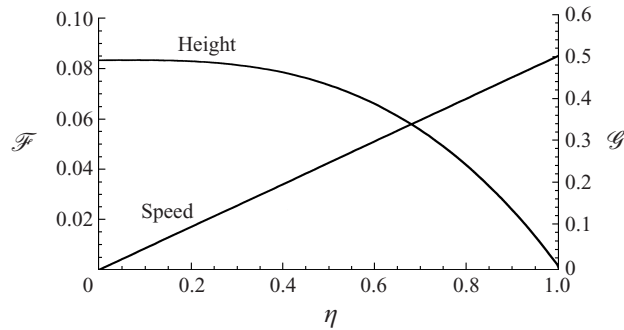
FIGURE 1. The dimensionless current depth, $\mathscr{F}(\eta)$, and speed, $\mathscr{G}(\eta)$, as a function of the dimensionless position, η, for a finite-volume release of fluid, $\gamma = 0$.
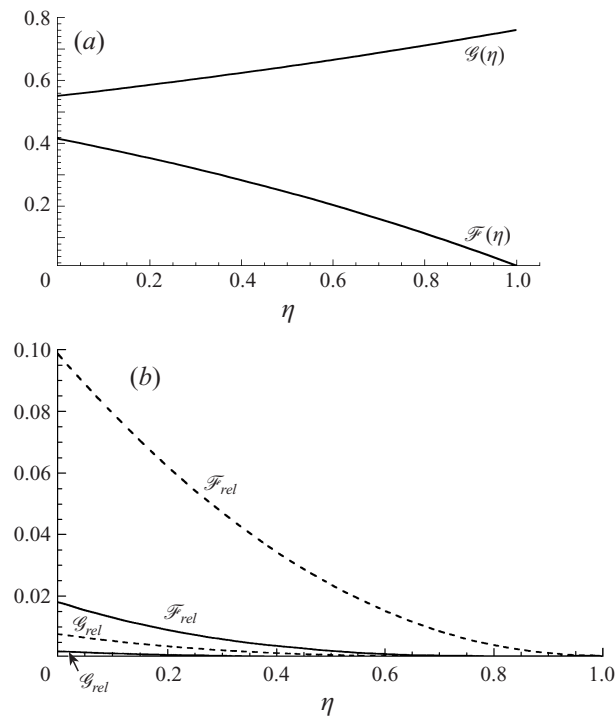

FIGURE 2. (a) Numerically calculated variation of the dimensionless current depth, $\mathscr{F}(\eta)$, and speed, $\mathscr{G}(\eta)$, as a function of the dimensionless position, η, for a constant flux of fluid at the source, $\gamma = 1$. (b) Relative errors of (i) the numerically calculated dimensionless current depth, $\mathscr{F}_{num}$, and the respective series approximation, $\mathscr{F}_{series}$; and (ii) the numerically calculated dimensionless speed, $\mathscr{G}_{num}$, and the respective series approximations, $\mathscr{G}_{series}$. For the case $\gamma = 1$. The dotted and solid lines are the relative errors when the series include terms up to $O((1-\eta)^2)$ and $O((1-\eta)^3)$ respectively.

for some constants $c_0, c_1, c_2, \ldots, d_0, d_1, d_2, \ldots$ We find $c_0 = 0$ since $\mathscr{F}(1) = 0$. Also, $d_0 = 1/2 + \gamma/4$ from condition (3.13). Substituting the power series into equations (3.8) and (3.9), and equating powers of $(1 - \eta)$ leads to values for the constants $c_1, \ldots, d_1, \ldots$. The first three terms in the expansion give the approximate solution

$$\mathscr{F}(\eta) = \left(\tfrac{1}{4}\gamma + \tfrac{1}{2}\right)^2 (1 - \eta) + \tfrac{1}{4}\left(\tfrac{1}{4}\gamma^2 - 1\right)(1 - \eta)^2$$
$$- \left(\tfrac{1}{144}(\gamma + 6)(\gamma - 2)\right)(1 - \eta)^3 + O((1 - \eta)^4), \tag{3.23}$$
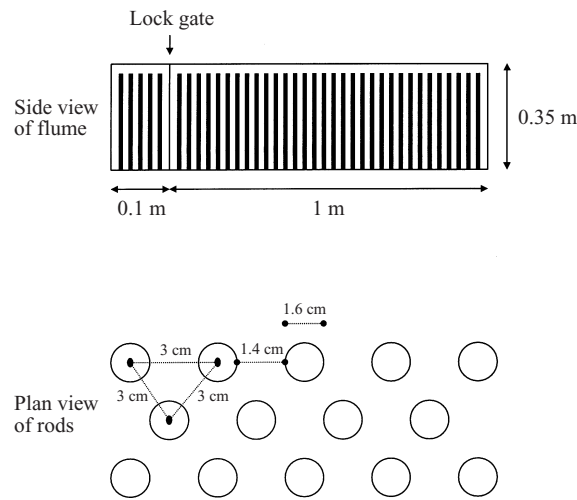
FIGURE 3. Schematic of the flume including the obstacles.

$$\mathscr{G}(\eta) = \left(\tfrac{1}{2} + \tfrac{1}{4}\gamma\right) + \tfrac{1}{2}\left(\tfrac{1}{2}\gamma - 1\right)(1 - \eta) + \tfrac{1}{6}\gamma\left(\frac{2 - \gamma}{2 + \gamma}\right)(1 - \eta)^2$$

$$+ \left(\frac{\gamma}{36}\frac{(7\gamma - 6)(\gamma - 2)}{(\gamma + 2)^2}\right)(1 - \eta)^3 + O((1 - \eta)^4). \qquad (3.24)$$

This approximate solution is in very good agreement with the solution obtained by the numerical integration of equations (3.8) and (3.9) as shown in figure 2(b) by the relative errors $\mathscr{F}_{rel} = |\mathscr{F}_{num} - \mathscr{F}_{series}|/\mathscr{F}_{num}$ and $\mathscr{G}_{rel} = |\mathscr{G}_{num} - \mathscr{G}_{series}|/\mathscr{G}_{num}$. In this figure the dotted lines show the relative errors when terms up to order $(1 - \eta)^2$ inclusive are retained and taken as an approximation to the full numerical solution. The solid lines show the relative errors when terms of order $(1 - \eta)^3$ are also included in the series approximation. This illustrates that the power series expansion converges very rapidly to the exact solution.

4. Experimental model

In the experiments we used a flume of length 3 m, width 0.153 m and depth 0.35 m with a lock gate placed 0.10 m from the endwall, $x = 0$. A regular array of vertical metal rods encased in plastic tubing, and mounted on a false floor of length 1.1 m was inserted into the flume. The rods had a diameter of 0.016 m and the centres of adjacent rods were 0.03 m apart, producing a gap between each adjacent pole of 0.014 m as depicted in figure 3. Using the flume, we conducted a series of finite-release experiments as shown in table 1. The main body of the flume was filled with fresh water, while the dyed saline fluid was placed behind the lock gate. Once the fluid motions had settled down, the lock gate was rapidly removed, and the motion of the gravity current was filmed by video camera and used for subsequent analysis.

In these experiments the drag coefficient for each cylindrical rod has value $c_D \sim 1$ (Rouse 1961); thus since the volume fraction occupied by the rods in the flume $\phi \sim 0.2$ and the diameter of the rods $d \sim 0.016$ m we expect that $\lambda \sim O(10)$. Therefore, with a current of finite volume $q_0 \sim 0.01$ m^2 per unit distance across the flume, and $g' \sim 0.1$ m s^{-2} we find that, from (2.6), $t_c \sim 1$ s so that the bulk of the experiment should be controlled by the regime of turbulent drag. Also, the viscous

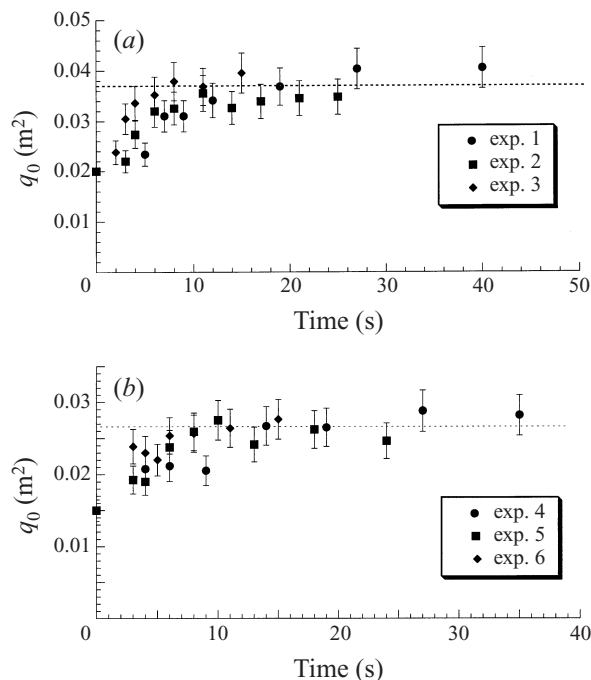| Experiment	$q_0(\text{m}^2)$	$g'(\text{m s}^{-2})$
1	0.020	0.0697
2	0.020	0.140
3	0.020	0.352
4	0.015	0.0697
5	0.015	0.140
6	0.015	0.352

TABLE 1. List of experiments.

FIGURE 4. The volume (per unit width) of the current as a function of time. The volume was estimated using the Digimage image processing system. (*a*) Experiments 1 to 3. (*b*) Experiments 4 to 6.

stresses from the floor of the tank and the rods are negligible for the typical flow speed of $0.02 - 0.2\,\text{m s}^{-1}$. Therefore, we expect that the model of §3 should provide a good description of the flows in these experiments.

5. Experimental results

We first monitored the degree of mixing of the flow with the ambient fluid. This was achieved by studying a video recording of the experiment, where the variation in area of the current with time was measured using the Digimage image processing system. It was found that immediately following the lock release there was rapid mixing, leading to dilution of the current by a factor of about 2. This initial mixing occurred as ambient fluid was rapidly engulfed into the dense intruding fluid. However, following this initial mixing, which occurred during the first few seconds after releasing the lock gate, the volume of fluid in the current remained approximately constant as shown
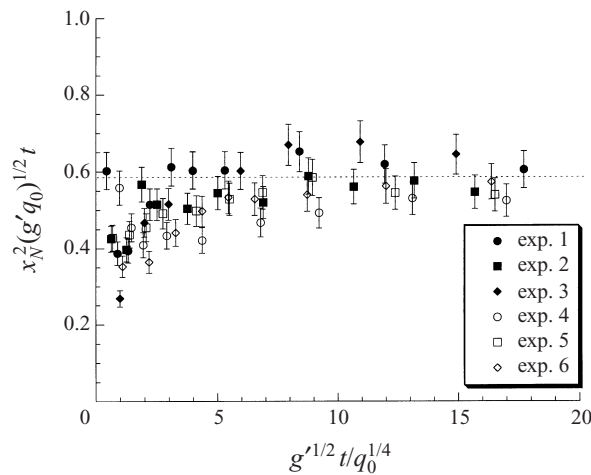
FIGURE 5. Ratio of the measured position of the leading edge of the current and the self-similar scaling for the position, $x_N^2/(g'q_0t^2)^{1/2}$, as a function of the dimensionless time $g'^{1/2}t/q_0^{1/4}$ for experiments 1 to 6.
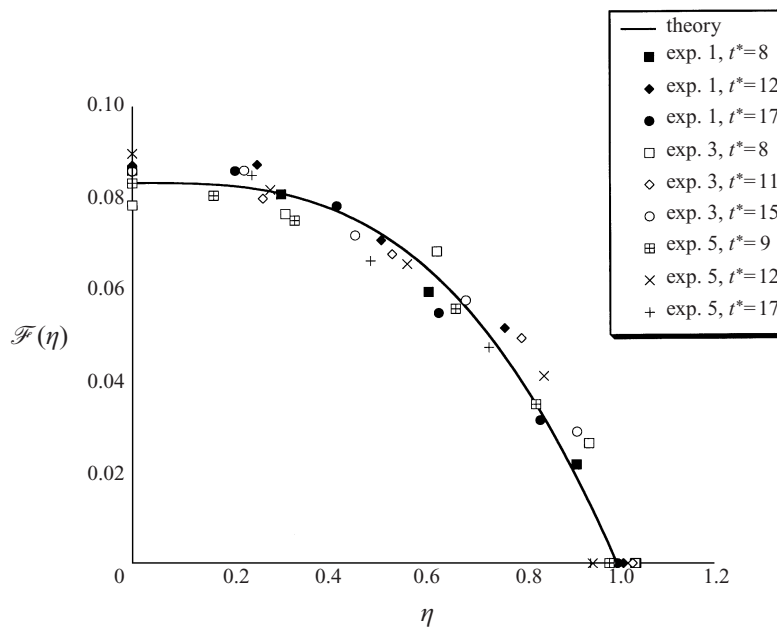
FIGURE 6. Comparison between the predicted dimensionless shape of the current, $\mathcal{F}(\eta)$ as a function of η and the dimensionless measured shape of the current at dimensionless times, $t^* = g'^{1/2}t/q_0^{1/4}$, for experiments 1, 3 and 5.

by figures 4(*a*) and 4(*b*). This suggests that during the main stage of spreading of the current, which persisted for 15–40 s, there was negligible entrainment of the overlying fluid and the current formed a low-aspect-ratio intrusion along the base of the flume. We note that the total buoyancy of the flow, q_0g', is conserved under this dilution and hence the progression of $x_N(t)$ is unaffected. However, the profile of the current is a function of dilution and hence we have quantified it for these experiments.

We then measured the rate of advance of the head of the current as a function of time. These measurements are shown in figure 5, where we plot the variation of $x_N^2/(q_0 g')^{1/2} t$ as a function of the dimensionless time $g'^{1/2} t/q_0^{1/4}$. In each experiment, after a short initial adjustment, the current length follows the scaling, from (3.16),

$$x_N = 2 \left(\frac{q_0 g'}{\lambda} \right)^{1/4} t^{1/2}, \tag{5.1}$$

suggesting that $\lambda^{-1/2} = 0.15 \pm 0.01$ and so for the array of vertical obstacles, $\lambda = 44 \pm 8$. This agrees with our order of magnitude prediction of λ in § 4.

We also measured the shape of the currents at several different times. Figure 6 illustrates how the shape of the current in experiments 1, 3 and 5 evolves with time. Dimensionless profiles are shown at dimensionless times after the opening of the lock gate. It is seen that over this time, the shape of the current is self-similar, and that it is in good accord with the theoretical prediction (3.20).

These experiments confirm that the dynamical balance between turbulent drag and a streamwise pressure gradient, (2.8), provide a very good description of the propagation of a turbulent gravity current through an array of obstacles for a finite-volume release.

6. The effect of a sloping bed

The analysis and experiments described above are restricted to flows over a horizontal boundary. In many situations, such as dense-fluid propagation in a fractured rock, the flow may advance down an impermeable slope, and it is of interest to examine the different behaviour of the flow in this case. The momentum equation now becomes

$$\frac{\partial u}{\partial t} + u \frac{\partial u}{\partial x} + g' \cos \theta \frac{\partial h}{\partial x} - g' \sin \theta = -\lambda u^2, \tag{6.1}$$

where θ is the angle of the slope to the horizontal. Therefore, for high-speed flow, sufficiently large drag, or at sufficiently long times, so that $t \gg t_c$ (cf. § 2), the drag force will dominate the inertial forces, and equation (6.1) will reduce to

$$g' \cos \theta \frac{\partial h}{\partial x} - g' \sin \theta = -\lambda u^2. \tag{6.2}$$

Substituting (6.2) into the mass conservation equation (2.1) gives

$$\frac{\partial h}{\partial t} + \frac{\partial}{\partial x} \left(h \sqrt{\frac{g' \sin \theta}{\lambda}} \left(1 - \cot \theta \frac{\partial h}{\partial x} \right)^{1/2} \right) = 0. \tag{6.3}$$

With long shallow gravity currents on a relatively steep incline, we expect that $\sin \theta \gg h_x \cos \theta$, so that the current depth only changes over distances large compared to the slope. In this case, neglecting terms of $O((\cot \theta h_x)^2)$ gives the approximate form for (6.3)

$$\frac{\partial h}{\partial t} + \frac{\partial}{\partial x} \left(h \sqrt{\frac{g' \sin \theta}{\lambda}} \left(1 - \frac{\cot \theta}{2} \frac{\partial h}{\partial x} \right) \right) = 0. \tag{6.4}$$

Equation (6.4) represents a wave equation for the disturbances, with wave speed $(g' \sin \theta/\lambda)^{1/2}$, and a nonlinear diffusive spreading of the wave about this mean flow. For a steady source of fluid, the flow will evolve towards a uniform thickness except at the head of the flow, where the flow depth adjusts to zero. For a finite release of
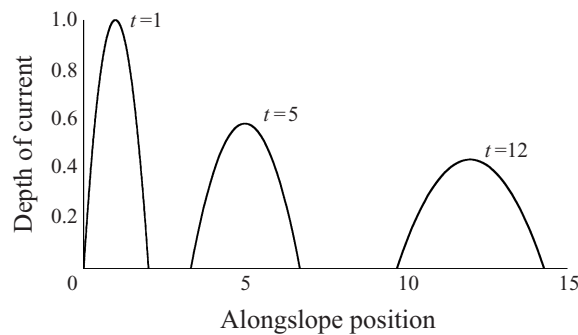
FIGURE 7. The theoretically predicted evolution of a finite release of fluid down a slope. The position and shape of the current are shown at three dimensionless times after the initial release.

fluid, such as occurs in an industrial explosion of dense gas or a snow avalanche, it is convenient to work in the frame moving with the wave speed, $U = \sqrt{g' \sin \theta / \lambda}$. We introduce new coordinates $X = x - Ut$ and $t = \tau$, so that the governing equation becomes

$$\frac{\partial h}{\partial \tau} - \frac{\cot \theta}{2} \sqrt{\frac{g' \sin \theta}{\lambda}} \frac{\partial}{\partial X} \left(h \frac{\partial h}{\partial X} \right) = 0. \tag{6.5}$$

This equation admits similarity solutions (cf. Pattle 1959) of the form

$$h(X, \tau) = X_0 H [\omega \tau]^\alpha \mathscr{F} \left(\frac{X}{x_N} \right) \tag{6.6}$$

where

$$x_N = X_0^{1/2} H [\omega \tau]^{1/3}, \quad \alpha = -\tfrac{1}{3} \tag{6.7a,b}$$

and

$$H = q_0^{1/2}, \quad \omega = \left(\frac{A^2}{q_0} \right)^{1/2}, \quad A = \cot \theta U / 2, \tag{6.8}$$

with $\mathscr{F}(\eta)$ satisfying the equation

$$-\frac{\mathrm{d}}{\mathrm{d}\eta}(\mathscr{F}\eta) = 3 \frac{\mathrm{d}}{\mathrm{d}\eta} \left(\mathscr{F} \frac{\mathrm{d}\mathscr{F}}{\mathrm{d}\eta} \right). \tag{6.9}$$

This has solution

$$\mathscr{F}(\eta) = \tfrac{1}{6}(1 - \eta^2) \tag{6.10}$$

with

$$X_0 = \left(\int_0^1 \mathscr{F} \, \mathrm{d}\eta \right)^{-2/3} = 9^{2/3}. \tag{6.11}$$

It is interesting to note that as a result of the nonlinear relationship between the current speed and the gravitational force, the resulting nonlinear diffusion equation of the current shape (6.5) is different from that on a horizontal boundary, for which there is no along-boundary force. Figure 7 illustrates how the current spreads out alongslope as a result of the component of gravity normal to the slope. In turn, this leads to the rather different scalings (6.7) compared to those of § 3.

7. Applications

This work was motivated by a number of geophysical applications, including high-Reynolds-number flow in a rough-walled fracture and flow of a dilute powder snow avalanche through an array of retarding mounds. We now consider conditions under which the dynamical regime described herein might apply to such flows, and we examine the implications on the propagation of the flow.

The buoyancy–turbulent drag flow regime represents an intermediate asymptotic regime, with an inertia–buoyancy balance applying at earlier times, $t \ll t_c$ given by equation (2.6), and a viscous–buoyancy balance applying at later times, $t \gg t_v$. In order that this intermediate regime develops, we require $t_c \ll t \ll t_v$. The time scale on which viscous forces become important depends upon the particular flow geometry. In the present experiments, the viscous drag from the floor of the tank becomes important at $t \sim t_{v1}$ when $12vu/h^2 \sim \lambda u^2$ where h is the flow thickness and v is the kinematic viscosity of the fluid. The viscous drag associated with the obstacles becomes important at $t \sim t_{v2}$ when $\phi vu/w^2 \sim \lambda u^2$ where w is the inter-obstacle spacing. Combining these relations with the self-similar drag-controlled flows, which apply for $t \ll t_v$, we find that

$$t_{v1} \sim \left(\frac{g'q_0}{\lambda}\right)^{1/2} \left(\frac{h^2\lambda}{12v}\right)^2 \tag{7.1}$$

and

$$t_{v2} \sim \left(\frac{g'q_0}{\lambda}\right)^{1/2} \left(\frac{w^2\lambda}{\phi v}\right)^2. \tag{7.2}$$

We note that $t_v = \min(t_{v1}, t_{v2})$.

7.1. *Rough-walled fractures*

In a rough-walled fracture, the size of the roughness elements will span a range of scales up to the fracture aperture, while they will be distributed throughout the fracture with some volume density ϕ which may lie in the range 0.001–0.1. The net effect of the roughness elements will be to produce a mean drag on a scale larger than that of the roughness elements. For high-Reynolds-number flow, the net frictional resistance associated with the roughness elements may be expressed in the form $\phi c_D u^2/y = \lambda u^2$ where y is the distance between fracture walls and c_D is an averaged drag coefficient, which accounts for the size distribution of the roughness elements.

For flow in a fracture there exists a third viscous time scale associated with the resistance of the bounding fracture walls, t_{v3} say, given by $12vu/y^2 \sim \lambda u^2$. Now

$$t_{v3} \sim \left(\frac{g'q_0}{\lambda}\right)^{1/2} \left(\frac{y^2\lambda}{12v}\right)^2 \tag{7.3}$$

and $t_v = \min(t_{v2}, t_{v3})$. In figure 8, we present calculations illustrating how the times t_c, from (2.6), and t_v vary with the volume release, q_0. For such a flow the viscous resistance is expected to be dominated by the viscous stresses associated with the fracture walls, so $t_v = t_{v3}$. It is seen that for small volume releases, $t_v \ll t_c$, there is a transition directly from the inertial flow regime to the viscous flow regime, so that the turbulent drag is not important. However, there is a critical $q_0 = q^*$, determined by the condition $t_c = t_v$ such that for $q_0 > q^*$, the flow dynamics are governed by the turbulent-drag-controlled regime for the period $t_c \lesssim t \lesssim t_v$. This is the flow regime which we have described in the above experiments and models.
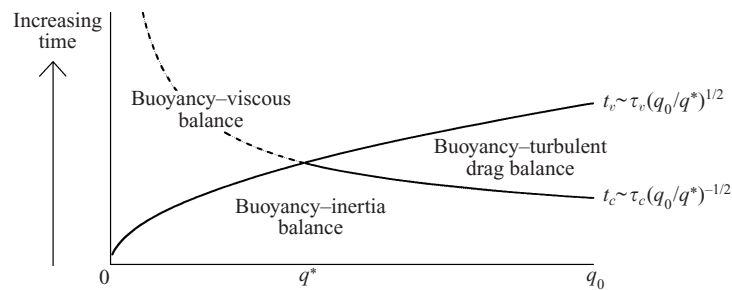
FIGURE 8. Illustrations of the evolution of high-Reynolds-number flow in a rough-walled fracture. The graph compares (i) the time at which the current inertia becomes comparable to the turbulent drag force on the flow, t_c; and (ii) the time at which the viscous resistance becomes comparable to the drag force, t_v. In the case $t_c < t_v$ the current passes through the intermediate asymptotic regime in which there is a balance between the turbulent drag and the gravitational acceleration. Otherwise, there is a direct transition from an inertial to a viscous gravity current.

The figure shows that for a large volume of injected liquid, the drag-controlled regime may apply for a considerable length of time, during which the current will spread far from the source. The region of fractured rock that is invaded by the liquid may then be quite different than would be predicted for inertial or viscous currents.

In the case that a finite flux of fluid is supplied to the current we expect that the liquid-saturated region near the source will continually deepen. In contrast, for an inertial gravity current, with a constant flux, the flow adjusts to a nearly constant depth, except at the flow front (Rottman & Simpson 1983). Therefore, we would expect a much deeper layer of liquid to form near the source if the effects of turbulent drag are dominant. Such considerations are crucial in applications such as the reinjection of liquid into superheated geothermal systems, for which the surface area of the flow has a key role in controlling the mass of liquid which boils (e.g. Woods 1999). They are also important in calculating regions of contamination following injection of pollutants into an aquifer.

7.2. Retarding mounds for snow avalanches

We can perform an analogous series of calculations for a snow avalanche channelled in a valley and passing through an array of obstacles. We consider the case in which the obstacles extend a considerable distance along the valley so that once the flow has entered the array of obstacles the turbulent drag associated with those obstacles is dynamically important. Although the initial interaction of the flow with the obstacles may lead to partial blocking of the flow and upstream propagation of a weak hydraulic jump (cf. Rottman *et al.* 1985) the subsequent evolution of the flow through the array of obstacles will be as described herein. If the obstacles are of size $d \sim 2\text{--}4\,\text{m}$, and occupy a fraction $\phi \sim 0.25$ of the flow path, then $\lambda \sim 1$. For an avalanche where $g' \sim 0.1$ and the initial size is $10^4\text{--}10^5\,\text{m}^2$ per unit distance in the cross-flow direction we predict that $t_c \sim 0.1\,\text{s}$ from (2.6) so the flow will be controlled by the drag–buoyancy balance soon after it has entered the array of obstacles. Using the typical characteristics of snow avalanches and retarding mounds, viscous stresses are negligible. For a finite volume release, the flow speed decreases inversely with the square-root of time, in contrast to inertia–buoyancy currents in which the flow speed decreases as $t^{-1/3}$. As a result, for an avalanche with the properties described above, the propagation speed may decrease more rapidly due to the drag, as seen in figure 9.
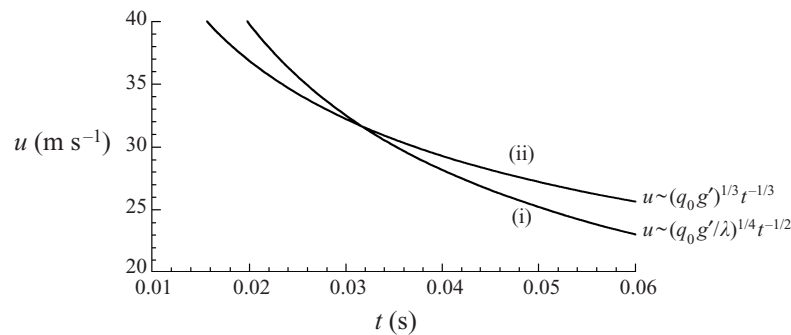
FIGURE 9. Variation of the speed as a function of time for a dilute snow avalanche propagating (i) through an array of retarding mounds; and (ii) in a simple inertial balance on a smooth horizontal boundary. Turbulent drag rapidly becomes dominant, leading to a reduction in flow speed at times $t \geqslant 0.03$ s.

If the mounds do not actually arrest the flow, then as a consequence of the drag they exert, they will reduce the impact of the avalanche on a building since the dynamic pressure of the flow will be smaller. A reduction in flow speed also reduces the ability to produce normal stresses which support the load of the granular flow. This may lead to more rapid sedimentation from the flow and hence dissipation of the flow. The present model provides an initial estimate of this reduction in the flow speed and hence the dynamic pressure.

8. Conclusions

We have developed a theoretical model which describes the behaviour of a gravity current subject to turbulent drag. Using scaling arguments, we showed that there is an intermediate asymptotic balance between the turbulent drag and the buoyancy force, with inertia dominating at short times and viscous resistance at longer times as shown in figure 8. Similarity solutions were derived to describe the motion of both constant-volume and constant-flux currents propagating along a horizontal boundary subject to this turbulent drag. New power series solutions for the shape of the current were developed, and shown to be very accurate representations of the numerically integrated profiles. The theoretical predictions were supported by a series of analogue laboratory experiments in which a flume, filled with vertical poles, was used to model the effect of retarding mounds on the propagation of a snow avalanche. Theoretical predictions for both the position of the nose and shape of the current were in very good accord with the experimental measurements. The model was extended to account for the effect of a slope, and a different set of scalings were shown to apply in that case. We note that the governing equations should be modified if the volume fraction ϕ is significantly larger than zero. The theory presented here assumes that the depth of the current is much smaller than the channel depth. A return flow in the upper layer may become important when the current occupies a substantial depth of the channel and the equations governing the motion should be altered accordingly. It is interesting to note that the phenomena we describe are closely related to the effects of turbulent bottom friction acting on a gravity current (Hogg & Woods 1999); however, since the frictional drag acts throughout the flow, the present model is much more amenable to verification by small-scale laboratory experiments.

Appendix. The effect of drag forces on an axisymmetric gravity current

A similar analysis can be carried out for an axisymmetric flow spreading from a point source. The derivation of these solutions closely follows §3 and so will not be presented in such detail. For an axisymmetric flow the analogous equations for mass and momentum conservation are

$$\frac{\partial h}{\partial t} + \frac{1}{r}\frac{\partial}{\partial r}(ruh) = 0 \tag{A1}$$

and

$$\frac{\partial u}{\partial t} + u\frac{\partial u}{\partial r} + g'\frac{\partial h}{\partial r} = -\lambda u|u|, \tag{A2}$$

where r is the radial coordinate. When the dominant dynamical balance is between the horizontal pressure gradient and turbulent drag, and $|u| = u$ so we have a purely outward radial flow, then (A2) reduces to

$$g'\frac{\partial h}{\partial r} = -\lambda u^2. \tag{A3}$$

The equation for global mass conservation is

$$\int_0^{r_N} 2\pi rh\,\mathrm{d}r = q_0 t^\gamma, \tag{A4}$$

where $\gamma \geqslant 0$ and q_0 is constant with dimensions of $L^3 T^{-\gamma}$. The system admits similarity solutions

$$h(r,t) = aH[\omega t]^\alpha \mathscr{F}(\eta), \tag{A5}$$

$$u(r,t) = bH\omega[\omega t]^\mu \mathscr{G}(\eta), \tag{A6}$$

where $\eta = r/r_N$, and $r_N = R_0 H[\omega t]^\beta$ is the position of the nose at time t. Furthermore, a, b and R_0 are multiplicative constants and dimensional consistency is enforced by the introduction of H and ω with dimensions $[H] = L$ and $[\omega] = T^{-1}$. Substitution of (A5) and (A6) into (A1), (A3) and (A4) gives

$$h \sim t^{(3\gamma-4)/5}, \quad u \sim t^{(\gamma-3)/5}, \quad r_N \sim t^{(2+\gamma)/5}. \tag{A7a,b,c}$$

For convenience we take $a = R_0^3$, $b = R_0$. Then, substituting α, β and μ into (A5) and (A6) we obtain the following differential equations for the shape and speed of the current:

$$\left(\frac{3\gamma-4}{5}\right)\mathscr{F} - \left(\frac{2+\gamma}{5}\right)\frac{\mathrm{d}\mathscr{F}}{\mathrm{d}\eta}\eta + \frac{\mathscr{F}\mathscr{G}}{\eta} + \frac{\mathrm{d}}{\mathrm{d}\eta}(\mathscr{F}\mathscr{G}) = 0, \tag{A8}$$

$$\frac{\mathrm{d}\mathscr{F}}{\mathrm{d}\eta} + \mathscr{G}^2 = 0, \tag{A9}$$

where we have set

$$H = \left(\frac{\lambda}{g'}q_0^{2/\gamma}\right)^{\gamma/(6-2\gamma)} \tag{A10}$$

and

$$\omega = \left(\frac{\lambda}{g'}q_0^{2/3}\right)^{3/(2\gamma-6)}. \tag{A11}$$

Hence

$$h(r,t) = R_0^3 \lambda^{2/5} g'^{-2/5} q_0^{3/5} t^{(3\gamma-4)/5} \mathscr{F}(\eta), \tag{A 12}$$

$$u(r,t) = R_0 \lambda^{-1/5} (q_0 g')^{1/5} t^{(\gamma-3)/5} \mathscr{G}(\eta) \tag{A 13}$$

where

$$r = \eta R_0 \left(\frac{q_0 g'}{\lambda} \right)^{1/5} t^{(2+\gamma)/5}. \tag{A 14}$$

Substituting the similarity solutions into the equation for global mass conservation gives

$$R_0 = \left(2\pi \int_0^1 \eta \mathscr{F} \, \mathrm{d}\eta \right)^{-1/5} \tag{A 15}$$

and the kinematic boundary condition

$$\frac{\mathrm{d}r_N}{\mathrm{d}t} = u(r_N) \Rightarrow \mathscr{G}(1) = \frac{2+\gamma}{5}. \tag{A 16}$$

A.1. *Series solutions*

For a finite release, $\gamma = 0$, equations (A 8) and (A 9) admit an analytical solution. (A 8) may be expressed in the form

$$-\frac{2}{5} \frac{\mathrm{d}}{\mathrm{d}\eta} \left(\mathscr{F} \eta^2 \right) + \frac{\mathrm{d}}{\mathrm{d}\eta} \left(\mathscr{F} \mathscr{G} \eta \right) = 0, \tag{A 17}$$

hence

$$\mathscr{G} = \tfrac{2}{5}\eta. \tag{A 18}$$

Upon substituting (A 18) into (A 9) and using the condition $\mathscr{F}(1) = 0$ we obtain

$$\mathscr{F} = 1 - \tfrac{4}{75}\eta^3. \tag{A 19}$$

When $\gamma > 0$ we again seek approximate series solutions of the form

$$\mathscr{F}(\eta) = c_1(1-\eta) + c_2(1-\eta)^2 + \cdots, \tag{A 20}$$

$$\mathscr{G}(\eta) = \frac{2+\gamma}{5} + d_1(1-\eta) + d_2(1-\eta)^2 + \cdots, \tag{A 21}$$

for some constants $c_1, c_2, \ldots, d_1, d_2, \ldots$. Upon substituting (A 20) and (A 21) into (A 8) and (A 9) and equating powers of $(1-\eta)$ we find

$$\mathscr{F}(\eta) = \frac{(\gamma+2)^2}{25}(1-\eta) + \frac{(3\gamma-4)(2+\gamma)}{50}(1-\eta)^2$$
$$+ \left(\frac{17}{900}\gamma^2 + \frac{2}{225}\gamma + \frac{4}{75} \right)(1-\eta)^3 + O((1-\eta)^4), \tag{A 22}$$

$$\mathscr{G}(\eta) = \frac{2+\gamma}{5} + \frac{3\gamma-4}{10}(1-\eta) + \frac{\gamma(8-\gamma)}{12(2+\gamma)}(1-\eta)^2$$
$$+ \frac{\gamma(43\gamma^2 - 68\gamma + 192)}{144(2+\gamma)^2}(1-\eta)^3 + O((1-\eta)^4). \tag{A 23}$$

Note that the term $\mathscr{F}\mathscr{G}/\eta$ in (A 8) was dealt with by writing $1/\eta = 1/(1-(1-\eta))$ and then using the binomial expansion. For a constant flux, $\gamma = 1$, the series gives a good approximation near the nose of the current, however, near the source, $\eta = 0$,

the depth of the flow predicted by this series diverges from the numerically calculated solution. In fact, near the origin, the constant flux supplied at $\eta = 0$ requires that $\mathscr{F}(\eta) \sim \eta^{-\frac{1}{3}}$. This divergence at the origin may be patched to the series solution near the nose of the current.

Validity of the solution

As in the unidirectional case the similarity solutions are only valid at intermediate times when the turbulent drag dominates both the current inertia and the viscous resistance. As before, for inertia to be small, we require

$$\lambda u^2 \gg \frac{\partial u}{\partial t}. \tag{A 24}$$

Upon substituting in the similarity solutions we find that turbulent drag dominates inertia if

$$t \gg t_c \sim (R_0^5 \lambda^4 q_0 g')^{-1/(2+\gamma)}. \tag{A 25}$$

Turbulent drag dominates the viscous resistance associated with the obstacles if

$$\lambda u^2 \gg \frac{\phi v u}{w^2} \tag{A 26}$$

where ϕ is the volume fraction occupied by the obstacles and w is the inter-obstacle spacing. Substituting in the similarity solutions we find that this is satisfied if

$$t \ll t_v \sim \left(\frac{\phi v}{R_0 w^2 \lambda^{4/5} (q_0 g')^{1/5}} \right)^{5/(\gamma-3)}, \tag{A 27}$$

so the turbulent drag solutions apply when $t_c \ll t \ll t_v$.

REFERENCES

BEAR, J. 1988 *Dynamics of Fluids in Porous Media*. Dover.

DULLIEN, F. A. L. 1991 *Porous Media – Fluid Transport and Pore Structure*. Academic.

ELLISON, T. H. & TURNER, J. S. 1959 Turbulent entrainment in stratified flows. *J. Fluid Mech.* **6**, 423–448.

GILL, A. E. 1982 *Atmosphere–Ocean Dynamics*. Academic.

GRATTON, J. & VIGO, C. 1994 Self similar gravity currents with variable inflow revisited: plane currents. *J. Fluid Mech.* **258**, 77–104.

HOGG, A. J. & WOODS, A. W. 1999 The transition from inertia to bottom drag dominated motion of turbulent gravity currents. (In preparation.)

HOPFINGER, E. J. 1983 Snow avalanche motion and related phenomena. *Ann. Rev. Fluid Mech.* **15**, 47–76.

HOULT, D. P. 1972 Oil spreading on the sea. *Ann. Rev. Fluid Mech.* **4**, 341–368.

JÓHANNESSON, T., LIED, K., MARGRETH, S. & SANDERSON, F. 1996 An overview of the need for avalanche protection measures in Iceland. Report prepared for the Icelandic Ministry for the Environment and local authorities in towns threatened by avalanches. Reykjavik.

LANE-SERFF, G. F. 1993 On drag-limited gravity currents. *Deep-Sea Res.* I **40**, 1699–1702.

LANE-SERFF, G. F., BEAL, L. M. & HADFIELD, T. D. 1995 Gravity current flow over obstacles. *J. Fluid Mech.* **292**, 39–53.

PATTLE, R. E. 1959 Diffusion from an instantaneous point source with a concentration deposition co-efficient. *Q. J. Mech. App. Maths* **12**, 407–408.

ROTTMAN, J. W. & SIMPSON, J. E. 1983 Gravity currents produced by instantaneous releases of a heavy fluid in a rectangular channel. *J. Fluid Mech.* **135**, 95–110.

ROTTMAN, J. W., SIMPSON, J. E., HUNT, J. S. R. & BRITTER, R. E. 1985 Unsteady gravity currents over obstacles. *J. Hazardous Mat.* **11**, 325–340.

Rouse, H. 1961 *Fluid Mechanics for Hydraulic Engineers*. Dover.

Simpson, J. E. 1997 *Gravity Currents in the Environment and the Laboratory*. Cambridge University Press.

Woods, A. W. 1999 Liquid and vapour flow in superheated rock. *Ann. Rev. Fluid Mech.* **31**, 171–199.